Chemical Engineering Journal 158 (2010) 61–68

Contents lists available at ScienceDirect

Chemical Engineering Journal

journal homepage: www.elsevier.com/locate/cej

Wavelet enhanced visualization of solids distribution in the top of a CFB

X. Xiong[a], Z. Zhang[a], S. Liu[b,*], J. Lei[c]

[a] National Natural Science Foundation of China, 83 Shuangqing Road, Haidian District, Beijing 100085, China
[b] Key Laboratory of Condition Monitoring and Control for Power Plant Equipment, Ministry of Education, North China Electric Power University, Beijing 102206, China
[c] Institute of Engineering Thermophysics, Chinese Academy of Sciences, P.O. Box 2706, Beijing 100080, China

ARTICLE INFO

Article history:
Received 18 July 2008
Received in revised form
18 December 2009
Accepted 21 December 2009

Keywords:
ECT image reconstruction
Flow visualization
CFB

ABSTRACT

In a circulating fluidized bed (CFB) the cross-sectional solids distribution in the top zone may differ from that in the lower zones. Particularly, the solids concentration distribution around the exit could be noticeably higher than that in other places. As an important factor affecting heat transfer in CFBs, cross-sectional solids concentration has rarely been investigated by means of online process tomographic (PT) visualization. This work uses electrical capacitance tomography (ECT) to visualize the solids distributions in the top zone of a CFB. In addition, wavelet methods are used for de-noising and image enhancement, and the effects are found in three aspects: (1) the influence of noise in the raw data can be reduced, which improves the quality of the reconstructed images; (2) the noise in the reconstructed ECT images can be reduced, providing a means for further image enhancement; (3) the rough patches of the images can be visibly smoothed, which is valuable for image refinement under coarse image pixel divisions. Experimental data revealed important features of the solids distribution, including (1) the core-annulus flow pattern, (2) the high solids concentration in the corners of the riser, (3) the moderate effect of the cap of the riser, and (4) the high solids concentration near the exit.

1. Introduction

Solids distribution in the top zone of a circulating fluidized bed (CFB) is one of the very important factors that influence strongly the heat transfer rate. Skewed solids concentration profile has been observed around the exit of the riser. However, this has not been clearly visualized by cross-sectional concentration measurement. Due to the opaque nature and erosive environment, it is very difficult for conventional methods to perform such a measurement.

Electrical capacitance tomography (ECT) was developed in the 90s of the last century [1], and has been under rapid development in recent years. Yet ECT is not a mature technology and its applications are appliance-dependent, i.e. the sensor design, calibration, and data interpretation, etc., depends on the understanding of the specific dielectric and geometric properties of the objects for ECT measurement.

ECT has been used successfully in the measurement of the solids distributions in the lower part of CFBs where the solids concentration usually exceeds 20–30% [2]. However, a particular problem for ECT is the very low solids concentration in the top of a CFB combustor. For example, in a CFB combustor, the solids concentration in the top part can often be lower than 2–3%. ECT measurements under such a condition tend to produce signals with very low signal-to-noise ratio, resulting in low image quality. Therefore, effective image reconstruction algorithms and noise reduction methods are of vital importance for accurate measurements.

Wavelet methods, or similar techniques, have been proven effective in noise reduction and image refinement [3–6]. Although they have been widely applied in other fields, their advantages in ECT image enhancement and de-noising have not been fully implemented. It is one of the main motivations of this work to explore the effects of the wavelet methods, in association with ECT image reconstruction methods, for the visualization of dilute solids concentration in the vicinity of the exit of CFBs.

In this study, ECT technology is used to investigate the solids distributions in the top zone of a model CFB combustor; meanwhile, the characteristics of the wavelet method in de-noising and image enhancement for ECT image reconstruction are also explored.

2. ECT image reconstruction

There are two major computational aspects in the image reconstruction for ECT: the forward problem and the inverse problem. The forward problem in ECT determines the inter-electrode capacitances from the permittivity distribution inside the interrogated zone, while the inverse problem aims to determine the material distribution from the measured capacitance values. The results can also be presented as visual images, and hence this process is called

* Corresponding author. Tel.: +86 1051963937; fax: +86 1051963937.
E-mail address: liushi_ncepu@yahoo.com.cn (S. Liu).

1385-8947/$ – see front matter © 2010 Elsevier B.V. All rights reserved.
doi:10.1016/j.cej.2009.12.031

image reconstruction. Suppose in a measurement m capacitance data are acquired and the image is divided into n pixels, in practice, the model of image reconstruction is often expressed by the following matrix equation [7]:

$$\boldsymbol{SG} = \boldsymbol{C} \tag{1}$$

where $\boldsymbol{C}$ is an $m \times 1$ dimensional vector indicating the capacitance values; $\boldsymbol{G}$ is an $n \times 1$ dimensional vector standing for the permittivity distribution, or in other words the material distribution; $\boldsymbol{S}$ is a matrix of dimensions $m \times n$, often called the sensitivity matrix, or sensitivity map [2].

The task of inverse problems of ECT is finding $\boldsymbol{G}$ from known $\boldsymbol{S}$ and $\boldsymbol{C}$. There are three major difficulties with image reconstruction in ECT [8]: (1) in reality the relationship between the permittivity distribution and capacitance is non-linear and the electric field is distorted by the material, this is the so-called "soft field" effect [2]; (2) the number of independent measurement data is usually far fewer than that of the pixels in the reconstructed image, i.e. available data are far fewer than what need to be decided; (3) the inverse problem is ill-posed and ill-conditioned. The solution is very often unstable and sensitive to noise in the input data.

One of the most commonly used image reconstruction algorithm is the Linear Back Projection (LBP). Based on Eq. (1), LBP method can be expressed by:

$$\boldsymbol{G} = \boldsymbol{S}^T\boldsymbol{C} \tag{2}$$

The advantages of LBP are numerical simplicity and high computational speed because it only involves a single matrix-vector multiplication. However, the quality of the reconstructed image is relatively low for complex object distributions. Various methods are available to improve the quality of reconstructed images, and more details can be found in [8]. Currently, iterative algorithms are often very effective. One of the successful iteration algorithms is the Landweber algorithm [7,9,10] expressed as:

$$\boldsymbol{G}_0 = \boldsymbol{S}^T\boldsymbol{C} \tag{3}$$

$$\boldsymbol{G}_{k+1} = \boldsymbol{G}_k + \alpha_k\boldsymbol{S}^T(\boldsymbol{C} - \boldsymbol{S}\boldsymbol{G}_k) = \boldsymbol{G}_k + \alpha_k\boldsymbol{S}^T\boldsymbol{r}_k \tag{4}$$

where k is the iteration step. In each step $\boldsymbol{G}_k$ is modified by adding $\alpha_k\boldsymbol{S}^T(\boldsymbol{C} - \boldsymbol{S}\boldsymbol{G}_k)$ to form a new $\boldsymbol{G}_{k+1}$. The expression $\boldsymbol{r}_k = (\boldsymbol{C} - \boldsymbol{S}\boldsymbol{G}_k)$ is the error between the measured capacitance $\boldsymbol{C}$ and the simulated capacitance value $\boldsymbol{S}\boldsymbol{G}_k$. α_k is a relaxation factor, or the step length. The iteration is repeated until a certain stop criterion is met [10].

A drawback of iterative methods is the cost of time. One of the remedies for this problem is the authors' recently derived OIOR algorithm [11,12], described by:

$$\boldsymbol{D}_0 = \boldsymbol{S}^T \tag{5}$$

$$\boldsymbol{D}_{k+1} = (I - \alpha_k\boldsymbol{S}^T\boldsymbol{S})\boldsymbol{D}_k + \alpha_k\boldsymbol{S}^T \quad (k = 1, 2, \ldots, z), \tag{6}$$

$$\boldsymbol{G} = \boldsymbol{D}_z\boldsymbol{C} \tag{7}$$

The algorithm is executed in two stages. The first stage is an offline process, in which Eq. (6) is iterated for z times and a coefficient matrix $\boldsymbol{D}_z$ is generated, where z can be decided in the same way as for the Landweber algorithm. In the second stage, $\boldsymbol{D}_z$ is used for online image reconstruction by Eq. (7). The algorithm improves images in the same way as the Landweber method. However in OIOR the coefficient matrix $\boldsymbol{D}_k$ is updated offline thus will not delay image reconstruction during online measurement. Furthermore, the algorithm does not involve a regularization parameter that is often difficult to determine [13]. Due to the above merits, OIOR is chosen for the current study.

In addition to the above linear methods, non-linear methods are also advantageous in certain types of applications. Because the current study is not focused on the development of image reconstruction methods, therefore, linear methods are adopted for faster image reconstruction speed and easier implementation, and the effects of non-linear methods will be investigated in further studies.

3. Wavelet technique

Wavelet analysis is an effective method for signal or image processing that has found a wide range of applications in physics, signal or image processing and applied mathematics [6]. In practice, wavelet analysis includes mainly two aspects: decomposition and reconstruction. Decomposition is a process where a signal or an image is decomposed into the wavelet space, which includes the detail components containing high frequency information, and the approximate components containing low frequency information. In the reconstruction process a signal or an image is reconstructed by both the approximate components and the de-noised detail components [6].

3.1. Wavelets considered

Often adopted wavelet functions include the Haar wavelet, the Daubechies wavelet, the Mexican Hat wavelet, the Morlet wavelet, the Biorthogonal wavelet, Complex Shannon wavelet, etc. The purpose of this study is to probe the effects of a wavelet method with ECT applications, rather than searching for an optimal wavelet function. Therefore, at this stage, we only consider several commonly used wavelets, namely the Haar wavelet, the Daubechies wavelet and the Biorthogonal wavelet.

The Haar wavelet $\psi_{Ha}(x)$ is the simplest wavelet. It was the first known wavelet and was proposed in 1909 by Aifred Haar. This wavelet is a step function:

$$\psi_{Ha}(x) = \begin{cases} 1, & 0 \le x \le 1/2 \\ -1, & 1/2 < x \le 1 \\ 0, & other \end{cases} \tag{8}$$

The Daubechies wavelet was invented by Ingrid Daubechies. The Daubechies wavelets $\psi_{DbN}(x)$, where N is the order, are compactly supported wavelets with extremal phase and highest number of vanishing moments for a given support width. Associated scaling filters are minimum-phase filters. In general these wavelets are not symmetric. They have no explicit expression except for $N = 1$.

The Biorthogonal wavelet family uses in fact two wavelets, one for decomposition and the other for reconstruction, instead of the same one like the Daubechies wavelet transform.

3.2. Wavelet de-noising and image enhancement

Practically, the reconstructed images may contain artefacts or errors due to the noises in the measured capacitance data, the unsuitable selection of parameters (especially regularization parameters), the spread and accumulation of errors during numerical iterations, etc. Therefore, it is desirable to carryout both post-processing of the reconstructed images and noise-reduction for the raw data for improved results. Wavelet techniques are considered for these purposes.

Images or signals containing noise can be expressed as $\boldsymbol{f} = \boldsymbol{f_T} + \boldsymbol{e}$, where $\boldsymbol{f_T}$ is a vector of the true values and $\boldsymbol{e}$ is a noise vector. The task of image or signal de-nosing is to recover the true values from the noisy values $\boldsymbol{f}$. According to the multi-resolution analysis [14–17], the property of a signal or an image can be described by the wavelet coefficients of orthogonal transformation, where the "large" coefficients correspond to the "true values", and the "small" ones represent mostly the noise. Therefore we can choose a threshold, e.g. s, and reserve the coefficients larger than s and discard those smaller than s. Then the signal or image is reconstructed using the reserved wavelet coefficients. When a suitable threshold is selected, this de-noising method may lose hardly any informa-

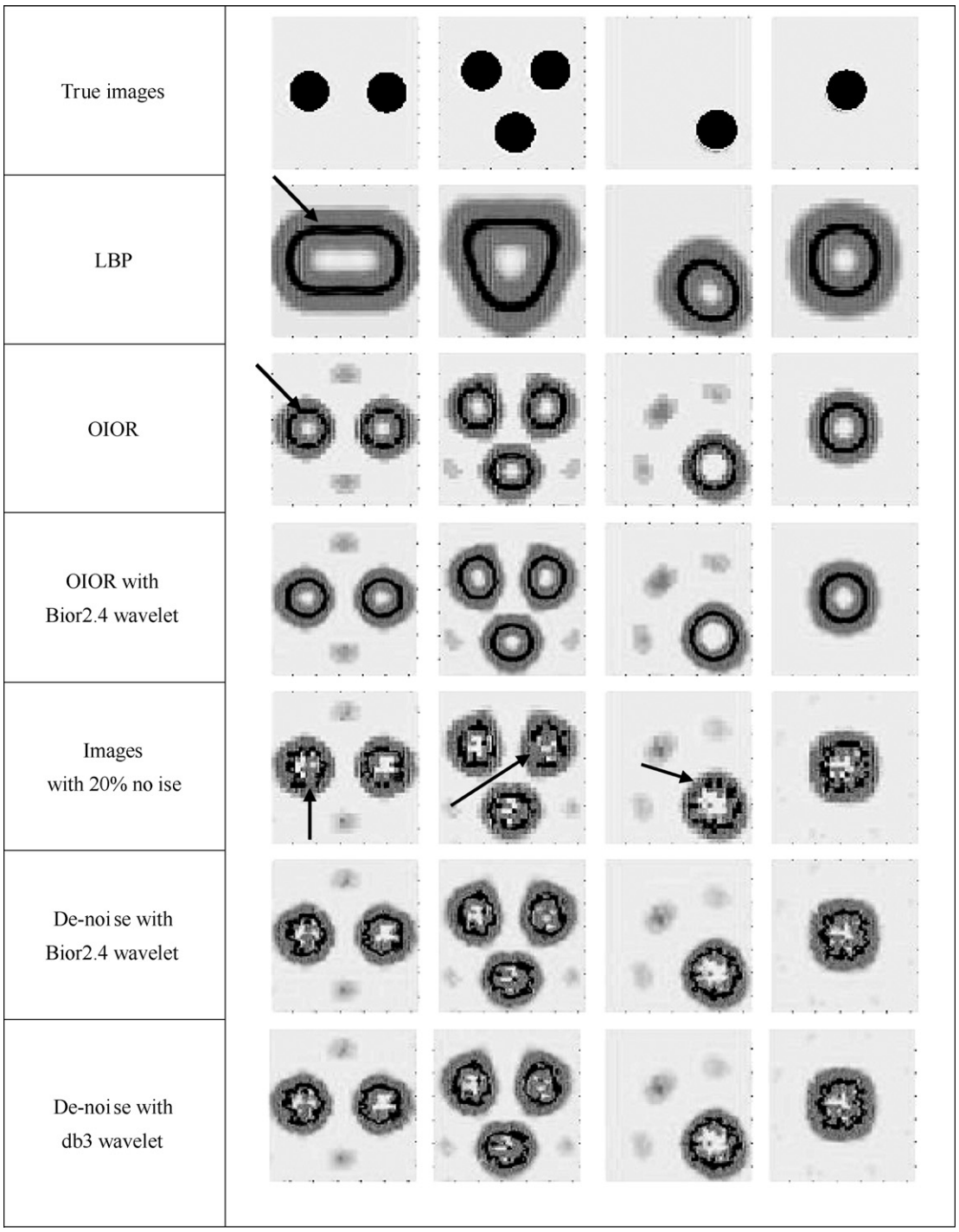

Fig. 1. Effect of wavelet de-noising on reconstructed images.

tion in the signal or image because the large coefficients contain nearly all characteristics of the signal or the image.

There are 3 steps for de-noising based on wavelet techniques [17,18]: (1) decomposition of the image or signal using a suitable wavelet function; (2) processing of the wavelet coefficients using a suitable thresholding scheme; (3) image or signal reconstruction using the reserved wavelet coefficients.

4. Image reconstruction and de-nosing

For convenience and clarity in the subsequent analyses, simulations are conducted to produce the images to reflect the effects of different algorithms. A commonly adopted squire sensor with 12 electrodes [2] is simulated; and images on a grid of 32×32 pixels are generated. LBP, OIOR and wavelet algorithms are facilitated by the software Matlab.

Four typical object setups are simulated. For each setup LBP and OIOR are used to reconstruct the initial images of the objects. Then noise is added to the images for the deterioration effects, and wavelet de-noising methods are applied afterwards to alleviate the deteriorations of the images. In addition, noise is also added to the capacitance data to simulate the noisy data acquired online.

The effects of the above mentioned algorithms are summarized in Fig. 1. The first row shows the setups of the objects. The black

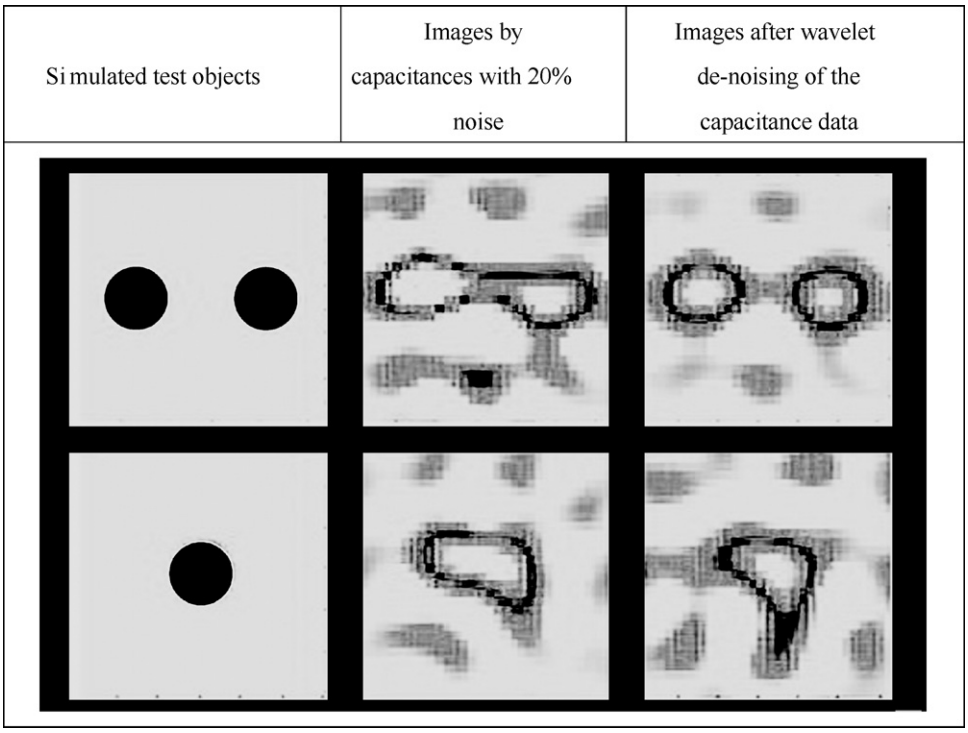

Fig. 2. Effect of wallet de-nosing on raw capacitance data.

circular images correspond to the objects having a relative permittivity of 2.6; and the rest denotes a free area with a low permittivity of 1.0. As the noise will tend to distort the images of the objects, attentions are thus focused on the boundaries of the images. Therefore, the ECT images in the following rows are further converted into gradient maps using software Photoshop7.0. Such maps assign different grey values (or different colors for a color map) according to the tonal values in the original images before the conversion. As the difference in tonal values are usually the largest across a boundary of an image, the sharpest changes of the grey value in the gradient map will therefore correspond to the boundaries of the original image. By this way, the boundaries of an image can be well distinguished.

Basic findings are as follows:

(1) For comparison purposes the second row shows the images reconstructed using LBP, one of the most basic algorithms. Apparently the two objects are not discriminated but encircled by one boundary, as pointed by an arrow. The low spatial resolution is one of the shortcomings of LBP.
(2) The third row listed the images reconstructed by OIOR algorithms. It can be seen that the boundaries of the images, one of them being indicated by an arrow, are well defined corresponding to the original object setups. With much improved spatial resolution yet fast speed, OIOR appears to be a favorable algorithm for this study.
(3) Even for the above simulated "noise-free" images, when wavelet de-noising is applied, visible improvement can also be seen. The fourth row demonstrates the images after Bior2.4 wavelet de-noising for the above OIOR images. In the images we can clearly seen that the boundaries are visibly smoothed, and the size of the "grains" in the images are also reduced.
(4) Now the noise is added to the OIOR images. It can be seen from the fifth row that after 20% noise is added to the images, the boundaries become significantly distorted, in some places the boundaries even break into discontinuous lines, as indicated by the arrows.
(5) Two wavelets, i.e. Bior2.4 and db3, are applied to reduce the noise effect in the above images. The de-noised images are listed in the sixth and seventh rows showing similar features. First, the boundaries of the images are largely restored and become continuous lines. Second, the grains in the images are somewhat smoothed as compared to the above.
(6) Finally, Fig. 2 shows the effect of wavelet de-noising for the contaminated raw data, i.e. the noisy capacitance data. By analyzing Fig. 2, it can be found that the quality of reconstructed images is enhanced when the noise in the raw capacitance data is reduced using the wavelet. As a result, it can be said that in general the effects of the wavelet techniques are significant.

5. Experiment and results

5.1. Experimental apparatus

As depicted by Fig. 3, the experimental apparatus is a CFB with one ECT sensor for bottom concentration measurement and another for the top at the exit level. As the upper part is the main subject of this investigation, measurement using the upper ECT sensor will be reported in this paper and the work on the bottom sensor will not be described. The riser is 2.8 m in height with a 140 mm × 140 mm cross section. Sands with a mean diameter of 0.28 mm and a material density of 2328 kg/m^3 are used as the bed material. The fixed bed is 200 mm before fluidization with a loosely packed voidage of 0.43. The superficial minimum fluidization velocity U_{mf} is 0.04 m/s [2]. The cross section on the upper ECT sensor level is depicted in Fig. 4. Sixty millimetres from the left wall is the exit with a width of 50 mm.

It has been noted that the height of the cap, i.e. the height of the portion above the exit, will affect the solids distributions in the top zone of a CFB. With the capability of ECT, in this work two different

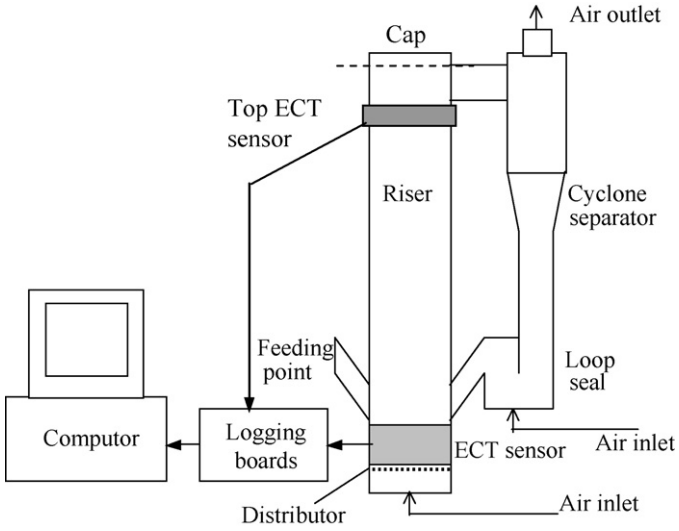

Fig. 3. Circulating fluidized bed and ECT sensor.

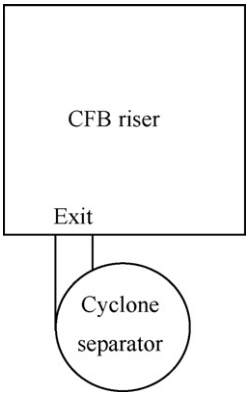

Fig. 4. Plan view CFB.

cap heights are used to investigate this effect. The height of the first cap is 160 mm and that of the second is 330 mm.

The upper ECT sensor is installed immediately below the exit of the fluidized bed to measure the solids concentration profile. The ECT device is an AC based logging system with a data collection speed of up to 140 frames per second [2]. The ECT sensor is depicted in Fig. 5. There are 12 electrodes, numbered from 1 to 12, attached to the outer wall of the riser that also serves as the frame of the sensor. A copper foil encloses the whole sensor as the shielding. The length of the electrodes is 100 mm, and the width of each electrode is 80 mm, with a gap of 2.5 mm between each pair of electrodes.

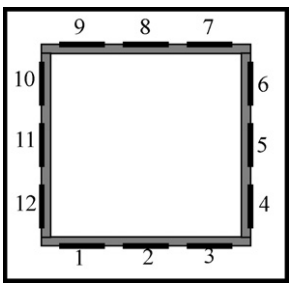

Fig. 5. ECT sensor.

5.2. Results and analysis

Solids concentrations over the cross section below the exit of the CFB are measured. The signals are processed using the Db3 wavelet for noise reduction and image refinement. This de-nosing process is carried out offline due to the amount of calculations being not suitable for online imaging. The images are displayed in Fig. 6. In the figure, 10 images are selected for both the low cap and the high caps as indicated in the figure. The number above each image indicates the frame in the series of reconstructed images. The time span between each frame will be the invert of the sampling speed, e.g. 0.025 s for a 40 fps sampling speed.

Analyzing Fig. 6, essential features are found as follows:

(1) The solids distribution presents an essentially core-annulus pattern: most solids are concentrated near the walls. This phenomenon has been identified for most CFBs, see, e.g. [19]; the measurement in this study provides further evidence for the top zone of CFBs.
(2) The corners tend to hold more solids. It is seen in most of figures that, apart from the exit, the corners of the riser seem to hold more solids than the other locations.
(3) Distinctively the solids concentration is higher near the exit, as indicated by the doted circle in the first figure. The measurement results agree with those in the literature, such as by Castilho and Cremasco [19], who stated that for the exit zone, the distributions show high values of solids holdup both near the wall and on the axis. Such a phenomenon could be the result of the stronger fluid drag that causes more solids to flow through a relatively narrow region near the exit.
(4) Comparing the images, it seems that the effect of the height of the cap is not very strong, which may implicatively agree with suggestions by Lackermeier and Werther [20], who measured the solids concentration by means of a two-channel fibre-optical probe, and found insignificant differences between the solids concentrations corresponding to a T-shaped exit (i.e. an equivalent to a high cap) and to an L-shaped exit (i.e. equivalent to low cap) on a much larger CFB.

    The effect of different shapes of the exits has been analyzed by Chen et al. [21] and outlined by Jin et al. [22]. According to their reports, an L-shaped exit was said to result in "higher solids concentration" at the riser top, and a T-shaped exit would be more restrictive and also produce higher solids concentration at the riser top. This type of effects were also commented by Lackermeier and Werther [20] as a phenomenon usually related to small rigs, and will not be significant with large rigs. The images from our ECT visualization seem to agree more with the latter.
(5) It is shown that the grey levels in the images vary in a rather smooth way without coarse patches, indicating the smoothing effect of the wavelet de-noising.

    Most of the above features can be seen more clearly if the ECT data are plotted in Matlab surface maps, i.e. 3D representations of the data. This is demonstrated in Fig. 7, in which we select 5 representative frames, numbered 1, 250, 500, 750 and 1000, from 1000 images collected in one experimental run. The images are represented using an 80×80 pixel division. The ordinate ranges from 0 to 255, i.e. in an 8 bit grey level scale, representing 0% to the maximum (i.e. full range) concentration of solids.

Analyzing Fig. 7, it can be seen clearly that: first, the core-annulus structure of solids distribution generally maintains; second, the solid concentration very often has a high peak in the vicinity of the exit (indicated by the arrows). In fact, solid distributions in the other images also follow the same pattern.

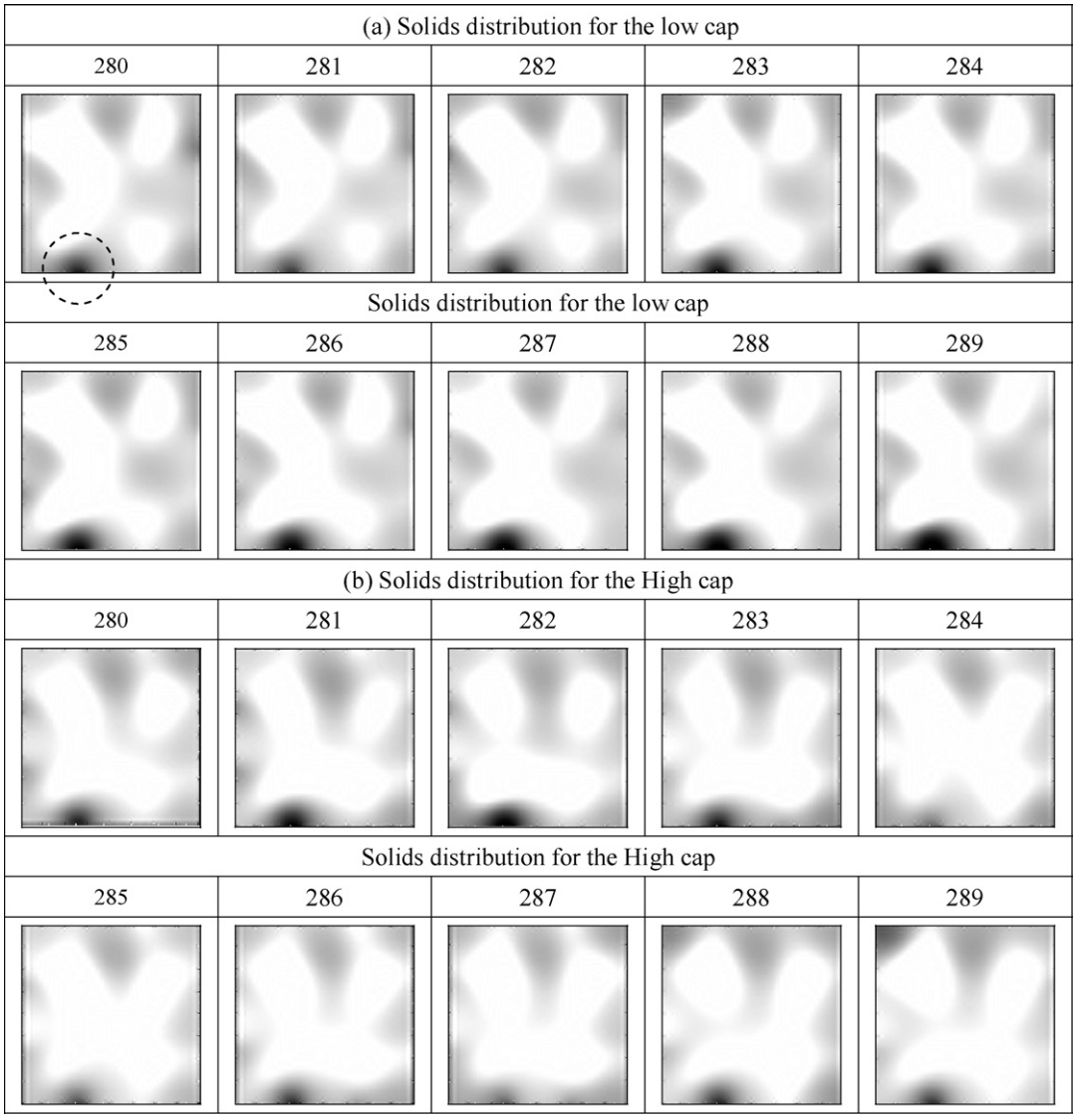

Fig. 6. Solids concentration immediately below the exit of the CFB riser.

In addition to the above, measurements were also carried out with a cap of an intermediate height 180 mm. The running conditions remained the same as the previous test. The lateral solids concentration distributions are presented in Fig. 8. Instead of filled maps, contour maps are used to reveal more details of the distribution. Compared with the previous measurements shown in Fig. 6, it can be seen that all the basic features largely remain, i.e. the core-annulus pattern, higher solids concentration in the corners, higher solids concentrations near the exit. Therefore, different heights of the caps may not cast distinctively different influence. Examining the concentration contours, the highest concentration can be found of a value around 60, and occasionally 80. As in our case the value 256 corresponds approximately to loosely packed solids concentration of 57%, the contour values of 60–80 indicate the highest local solids concentration of 13.4%, and occasionally 17.8%, respectively in a very small region just below the exit of the riser, albeit the average solids concentration remains relatively low over the cross section. A recent investigation by Wang et al. [23] on a dense fluidized bed reactor also indicated a rather high solids concentration in the upper part of the riser, due to the reflux effect, with even

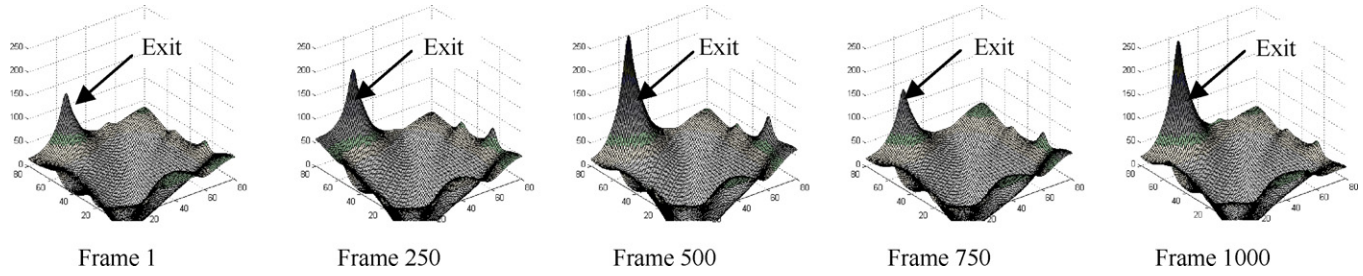

Fig. 7. High concentration of solids distribution near the exit of the riser of CFBs.

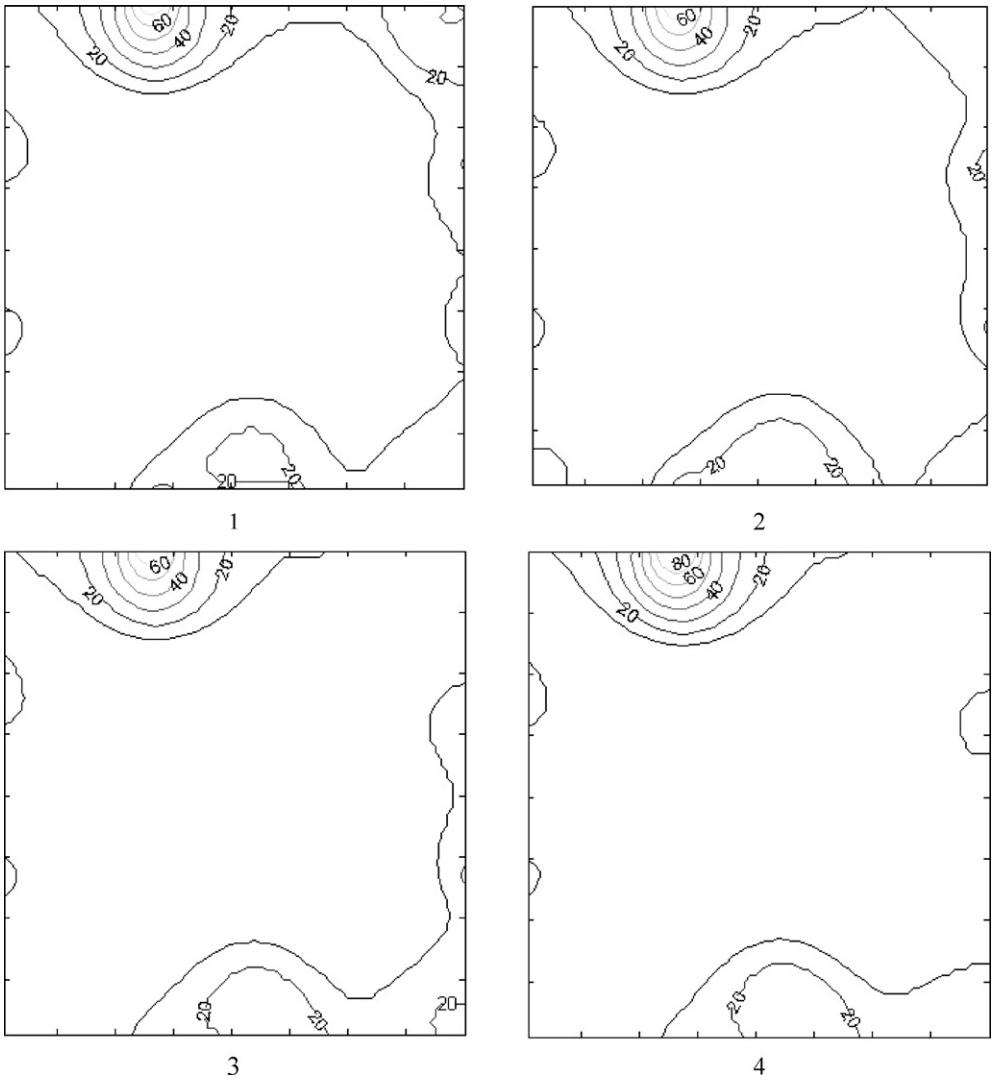

Fig. 8. Solids concentration immediately below the exit of the 180 mm cap CFB riser.

higher values on the wall than the ECT reconstructed values, which shows similar features of a CFB riser as used in this study.

6. Conclusions

ECT has been applied to visualize solid concentration distribution over the top cross section, and near the exit, of a CFB riser. Simulation results demonstrated the effects of the wavelet in noise reduction and image smoothing under coarse pixel division. For the comparatively low solid concentration in the CFBs that usually causes low signal-to-noise ratio in the ECT data, wavelet de-noising proves to be effective. Its effects are found in three aspects: (1) the influence of noise in the raw capacitance data can be reduced, which facilitates the reconstruction of higher quality images; (2) the influence of noise in the reconstructed ECT images can also be reduced, and the quality of the images can be enhanced; (3) the coarse patches in the images can be significantly smoothed, which is valuable for edge shape improvement of the reconstructed images under coarse pixel divisions.

The experimental data revealed basic characteristics of the solids distribution. First, the core-annulus flow pattern in the riser has been presented by ECT images. Second, high solids concentration in the corners of the upper part of the riser is also reflected by the ECT images. Third, the high solids concentration in the vicinity of the exit appears a noticeable feature, which is of particularly interests for the evaluation of heat transfer properties in the top zone of CFBs. Meanwhile, within the operating range of this study, acquired data suggest only moderate effect of the cap height on the overall solids concentration distributions, which provides a reference for further investigations on this matter.

The study is still in its preliminary stage, more simulations and experiments are needed to verify the findings of this study, and to improve the methods used here.

Acknowledgment

The authors wish to thank the National Natural Science Foundation of China for supporting this research project (Project No: 60672151, 60532020 and 50736002).

References

[1] C. Xie, S. Huang, B.S. Hoyle, R. Thorn, C. Lenn, D. Snowden, M.S. Beck, Electrical capacitance tomography for flow imaging: system model for development of image reconstruction algorithms and design of primary sensors, IEE Proc.-G 139 (1992) 89–97.
[2] S. Liu, H. Wang, F. Jiang, W.Q. Yang, A new image reconstruction method for tomographic investigation of fluidized beds, AIChE J. 48 (2002) 1631–1638.
[3] J.P. Antoine, R. Murenzi, P. Vandergheynst, S.T. Ali, Two-dimensional Wavelets and their Relatives, Cambridge University Press, Cambridge, 2004.

[4] R.M. Balabin, R.Z. Safieva, E.I. Lomakina, Comparison of linear and nonlinear calibration models based on near infrared (NIR) spectroscopy data for gasoline properties prediction, Chemometr. Intell. Lab. Syst. 88 (2007) 183–188.
[5] R.M. Balabin, R.Z. Safieva, E.I. Lomakina, Wavelet neural network (WNN) approach for calibration model building based on gasoline near infrared (NIR) spectra, Chemometr. Intell. Lab. Syst. 93 (2008) 58–62.
[6] K. Brudzewski, S. Osowski, T. Markiewicz, J. Ulaczyk, Classification of gasoline with supplement of bio-products by means of an electronic nose and SVM neural network, Sens. Actuators B 113 (2006) 135–141.
[7] W.Q. Yang, D.M. Spink, T.A. York, H. McCann, An image reconstruction algorithm based on Landweber's iteration method for electrical capacitance tomography, Meas. Sci. Technol. 10 (1999) 1065–1069.
[8] W.Q. Yang, L.H. Peng, Image reconstruction algorithms for electrical capacitance tomography, Meas. Sci. Technol. 14 (2003) 1–13.
[9] L. Landweber, An iterative formulafor Fredholm integral equations of the first kind, Am. J. Math. 73 (1951) 615–624.
[10] S. Liu, L. Fu, W.Q. Yang, Optimization of an iterative image reconstruction algorithm for electrical capacitance tomography, Meas. Sci. Technol. 10 (1999) 37–39.
[11] S. Liu, L. Fu, W.Q. Yang, H. Wang, F. Jiang, Prior on-line iteration for image reconstruction with electrical capacitance tomography, IEE Proc.-Sci. Meas. Technol. 151 (2004) 195–200.
[12] S. Liu, L. Fu, W.Q. Yang, F. Jiang, On-line iterative image reconstruction for ECT, in: Proceedings of the 3rd World Congress on Industrial Process Tomography, Bannff, Canada, 2003, pp. 403–408.
[13] A.N. Tikhonov, V.Y. Arsenin, Solution of Ill-posed Problems, V.H. Winston & Sons, Washington, 1977.
[14] J.C. Goswami, A.K. Chan, Fundamentals of Wavelet: Theory, Algorithm and Applications, John Willy & Sons, New York, 1999.
[15] I. Daubechies, Ten Lectures on Wavelets, SIAM Press, Philadelphia, Pennsylvania, 1992.
[16] S. Mallat, A Wavelet Tour of Signal Processing, Academic Press, San Diego, 1999.
[17] C. Xu, R.Z. Zhao, X.B. Gan, Wavelet Analysis: Applications and Algorithms, Science Press, Beijing, 2004.
[18] C.H. Hu, G.H. Li, T. Liu, Z.J. Zhou, Wavelet Analysis Based on the MATLAB 6.x, Xidian University Press, Xi'an, 2004.
[19] G.J. Castilho, M.A. Cremasco, Experimental study in a short circulating fluidized bed riser, Part. Sci. Technol. 27 (2009) 210–221.
[20] U. Lackermeier, J. Werther, Flow phenomena in the exit zone of a circulating fluidized bed, Chem. Eng. Process. 41 (2002) 771–783.
[21] Y. Jin, J. Zhu, Z. Yu, Novel configurations and variants, in: J.R. Grace, A.A. Avidan, T.M. Knowlton (Eds.), Circulating Fluidized Beds, Blackie Academic & Professional, London, 1997.
[22] Y. Chen, F. Wei, G. Yang, Y. Jin, Inlet and outlet effects on flow patterns in gas-solid risers, Powder Technol. 98 (1988) 151–156.
[23] X. Wang, F. Jiang, X. Xu, S. Wang, B. Fan, Y. Xiao, The simulation and experimental validation on gas–solid two phase flow in the riser of a dense fluidized bed, J. Thermal Sci. 18 (2009) 137–141.